About the Assessment of Heat Flux and Skin Friction of the DLR TAU-code for Turbulent Supersonic Flows

A. Kovar, V. Hannemann, S. Karl, E. Schülein
German Aerospace Centre, Göttingen, Germany

Abstract

The correct prediction of skin friction and surface heat flux by CFD tools is an important prerequisite for the design of hypersonic flight vehicles. Results of a test campaign of a flow past a flat plate configuration with an impinging oblique shock carried out in the Ludwieg Tube Facility of DLR Göttingen were used to assess the applicability and accuracy of the DLR TAU-code at respective flow conditions. A shock-wave/turbulent boundary layer interaction (SWTBLI) on the flat plate model was created with a planar shock generator at different incidence angles. This two dimensional test case involving the flat plate flow and the interaction of an oblique shock with the turbulent boundary layer is well documented with various measurements like wall pressure, boundary layer velocity profiles, skin friction, and heat flux, and offers a good basis for the assessment of the two latter variables for the DLR TAU-code. The assessment includes grid studies, the influence of various turbulence models as well as the external turbulence intensity set in the calculations.

Introduction

The heat loads on parts of hypersonic flight vehicles can be considerable. Control surfaces, inlets, or thermal protection systems have to be designed accordingly. Advanced numerical modelling techniques like direct numerical simulation (DNS) or large eddy simulation (LES) have emerged but their application to high Reynolds number flows is still associated with very high computational costs especially in boundary layers. The application of Reynolds-averaged Navier-Stokes (RANS) solvers is computationally more efficient but subject to uncertainties resulting from turbulence models, which were developed mainly for the incompressible flow regime. Hence, it is still a demanding problem for to date's CFD tools to predict the heat flux or the skin friction correctly. Especially, SWTBLI is a challenging task where also the correct prediction of the separation zone can not be taken for granted. This gave motivation to recalculate the well documented experiment [3, 7] that provides the required data to evaluate the numerically predicted heat flux and skin friction and the quality of the obtained solution. It was of special interest how the validity of the predicted quantities would depend on the boundary layer resolution, especially the wall normal grid spacing in terms of $y+$, on different turbulence models, and also on the external turbulent intensity set at the inflow boundary. Cases of different strengths of the interaction were investigated, ranging from a strong interaction with significant separation down to the case where a weaker interaction did not result in a separation. Four different RANS turbulence models were tested on these cases concerning their ability to simulate the flow parameters in agreement with the experiment.

Wind tunnel and experimental set-up and equipment

The experimental part of the investigation was conducted in the DLR Göttingen Ludwieg Tube Facility (RWG, Fig. 1), which covers a Mach number range of $2 \leq M \leq 7$ and a unit Reynolds number range of $2 \times 10^6 \leq Re_1 \leq 110 \times 10^6$ m^{-1}. The facility consists of a storage tube, which is separated from the test section and the dump tank by a fast reacting gate valve. If the gate valve is opened, an instationary expansion wave travels upward from the nozzle towards the storage tube, is reflected at its closed end and travels back downstream. The test conditions remain constant as long as the expansion wave does not reach the nozzle throat. The tube length of 80 m results in a run time of about 0.3 s. The experiments were conducted at a Mach number of $M = 5$, a unit Reynolds number of $Re_1 = 37 \times 10^6$/m, and a total temperature of $T_0 = 410$ K.

A flat plate of 300 mm in length and 400 mm in width was used as a shock generator for deflection angles of 6°, 10°, and 14° on the main flat plate of 500 mm in length and 400 mm in width as shown in Fig. 2. The shock generating plate was placed over the main flat plate so that a generated shock would impinge 350 mm from the leading edge independent of the shock generator angle. The main flat plate was instrumented with 10 individual ports for velocity measurements along its axis and 3 additional ports in spanwise direction as two-dimensionality check. The developing boundary layer was transitional with a natural transition to turbulent flow at about 100 mm downstream of the leading edge of the main flat plate.

The main flat plate was instrumented with 67 static pressure taps in different intervals from 2 to 20 mm along the centreline (taps 1-50) and crosswise (51-67). The taps were 0.3 mm in diameter and connected with short tubing length (≤ 150 mm) to a 32-port PSI ('Pressure Systems Inc.') pressure transducer module with a measurement range of ± 103400 Pa. An online three point pressure calibration is performed for all transducers before each measurement. The rated accuracy is quoted by the manufacturer to be of the order of ± 0.1 % full scale (about ± 100 Pa) or better.

Heat flux is determined via the thin-wall technique. This method can be applied in short-duration wind tunnels if the wall temperature normal to the model surface can be assumed uniform and the lateral heat conduction in the wall can be neglected. This is given for models manufactured from materials such as nickel used here, as they have sufficient high thermal conductivity and so the heat transfer between flow and model walls starts rapidly. The local heat flux rate $\dot{q}$ is directly calculated from the measured rise of the wall temperature T_w:

$$\dot{q} = \rho_m c_m d_m \frac{dT_w}{dt},$$

with c_m and d_m being material constants. The wall temperature was measured with thermocouples. The repeatability of this measurement technique is better than ± 5 %. More detailed information can be found in [7].

The skin friction was measured with the optical non-intrusive Global Interferometry Skin Friction (GISF) technique. The model surface is covered with an oil-film and exposed to the flow. The thinning of the oil film is related to the local surface shear. The thinning rate is determined from the optical interference that is created when an incident light beam is partially reflected by the oil and the test surface. The light source was a low-pressure sodium vapour lamp with an opal diffusing element between the light and the model surface. To improve the reflection properties of the model, a dark self-adhesive polyethylene foil was attached to it. The interferograms were recorded as a sequence of 8bit-gray-scale single images (1024×1024) using an ADIMEC 12XP charge coupled device camera at a rate of 30 frames/s. The error of the skin friction measurements depends mainly on the repeatability of the wind tunnel conditions and the viscosity of the oil. Here the error varies from ± 4 % in the undisturbed boundary layer up to ± 10 % in interaction zones. A more detailed description can be found in [7]. The experiment was already used for validation purposes and was also well examined in [1], [6], and [10].

The DLR TAU-code

The DLR TAU-code is a three-dimensional finite volume Euler / Navier-Stokes flow solver based on hybrid structured / unstructured grids ([2], [4], [8]). The advantage of a hybrid code is the combination of the benefits of structured grids to resolve wall heat transfer or wall shear stress with the ability of unstructured grids to efficiently improve the solution accuracy in flow regions of particular interest.

The TAU-code is composed of four independent modules: the pre-processor, the solver, the grid adaptation, and deformation. This modular design provides maximized flexibility for its application on parallel high performance computing (HPC) environments.

The TAU-code uses a second order finite-volume discretisation in space. Different central and upwind schemes (like AUSMDV) are implemented for sub- and transonic respectively super- and hypersonic flow. Several explicit Runge-Kutta schemes as well as an implicit LUSGS scheme are options to advance the solutions in time for steady flow fields. For convergence acceleration local time stepping, implicit residual smoothing and multigrid are implemented. Fast and accurate transient flow simulations are computed by an implicit Jameson type dual time stepping scheme. The TAU-code is validated for and applied to a wide range of flow conditions covering subsonic to hypersonic and high-enthalpy flows as well as combustion problems. Its extension for hypersonic flow field applications includes models to perform chemical and thermal equilibrium and non-equilibrium flow computations. In addition to a number of one- and two-equation eddy-viscosity turbulence models, Detached Eddy Simulation (DES) and a Reynolds Stress model are implemented in the code. In the field of high-enthalpy flows and hypersonics, TAU has been used for the CFD analysis of reacting high enthalpy flows past simplified test models ([2]) as well as complex re-entry configurations such as the Pre-X lifting body ([5]).

Due to the setup of this experiment, a 2-dimensional computational domain was chosen in order to reduce the computational cost for the parametric studies.

Prerequisites of the numerical calculations

Prior to the main investigation of the heat flux and skin friction, a grid refinement study was carried out to assure that the later initial grid already provides the necessary resolution in the boundary layer. As the heat flux is the most crucial parameter and tends to be the last to develop in a fully converged solution, this parameter was used as a check for grid convergence and independence. This was done on a simple flat plate without the shock generator, as the principal features have to be identified also in this simple case. Hence, three grids, a coarse, a medium, and a fine one, were created, which was sufficient to verify the grid independence of the predicted surface heat flux. The coarse grid contained 31,236 nodes, the medium grid 87,542 nodes, and the fine grid 246,006 nodes. The grids were created on the basis of the medium grid with 36 prismatic layers and a stretching of 1.18 resolving the boundary layer. For the resolution of the boundary layer of the coarse grid, the number of prismatic layers was reduced to 19 with a wall-normal stretching factor of 1.38 and for the fine grid the number of prismatic layers was doubled to 71 with a stretching factor of 1.09. The settings resulted in all grid cases in a wall-normal normalised coordinate y^+ of smaller than 0.2 and were varied to even smaller values throughout the process of adaptation.

Fig. 3 shows the surface heat flux distributions for the experiment and the three grids with different vertical resolutions in terms of the non-dimensional Stanton number St defined as

$$St = \frac{\dot{q}}{\rho_\infty U_\infty c_p \cdot (T_0 - T_w)} ,$$

where $\dot{q}$ is the heat flux, ρ_∞ and U_∞ are free stream density and velocity, c_p is the heat capacity at constant pressure, T_0 is the total temperature and T_w the temperature of the wall. The experimental data start at about x = 140 mm, where the flow is already fully turbulent. It becomes obvious that the coarse grid provides a slightly lower heat flux, whereas the medium and the fine grid don't show any differences anymore apart from the values close to the transitional area. Hence, for further calculations the medium sized grid was applied.

Another point that was concluded from the grid study is even more vital for the correct calculation of the heat flux in the undisturbed turbulent region. Most often grids are generated with a first wall spacing of y^+ = 1 for sufficient resolution of the boundary layer in the adiabatic sub- and transonic flow regime. For comparison, a calculation was performed on the medium grid but with a y^+ = 0.8 according to this described "usual procedure". As can be seen from Fig. 3, the heat flux drops substantially, if the y^+ is chosen around 1. As this was not the target, it cannot be concluded from this study what the limit is for a good resolution of the heat flux, this would be a point for a future study.

A third factor investigated on this grid study was the influence on external turbulent intensity. An additional calculation was conducted on the medium grid in which the external turbulent intensity was set to the according wind tunnel level, which corresponds to an increase from the default value of 0.1 % to the wind tunnel value of about 1.7%. It can be seen from the same graph (Fig. 3) that it is vital to set the turbulence intensity to the wind tunnel value (if available, which is not always the case), the calculation of the heat flux with the lower turbulence intensity does not reach the same level as in the experiment. Consequently, all in the following discussed calculations were performed on the medium grid with a y^+ of smaller than 0.2 and increased turbulence level of 1.7 %.

For the assessment of the skin friction, the experiment and the numerical calculation were compared with the turbulent solution according to Van Driest [3] on a simple flat plate (Fig. 4). It can be seen that while the Van Driest solution is approximating the experiment in the turbulent region, the numerical calculation shows a lack of shear stress for the whole length of the profile. Additionally, a laminar calculation was conducted and compared with an empirical approximation given by AD Young [9] shown on the same graph with a good agreement.

Results and Analysis

After the grid study, several turbulence models were tested on the case of an impinging oblique shock with a flow deflection angle of 14° creating a strong SWTBLI and the results were compared and analysed. An example of the shadowgraph images is given in Fig. 5 where the flow field is shown on the left and a superposition of the experiment and the numerical calculation is given on the right (numerical calculation in red). It can be seen that the flow topology is qualitatively captured. Deviations are visible in terms of the impinging shock position and the separation zone which will be discussed in the following. Afterwards, the knowledge gained from the results was applied on the cases of deflection angles of 10° and 6°. From the standpoint of interaction this is the strongest one and herewith the uncertainties should be the largest. The models tested encompassed the 1-equation model by Spalart-Almaras with Edwards modification (SA-E), 2-equation models, namely the Menter

SST (MSST), the TNT model developed by the NLR, and an algebraic Reynolds-stress model combined with a kω model by Hellsten, EARSM. As upwind solver the AUSMDV was applied for all cases. Data that were compared include the normalised boundary layer velocity profiles $u^+(y^+)$, normalised wall pressure P_w/P_1, normalised heat flux in terms of Stanton numbers St and the skin friction coefficient c_f.

The normalised velocity profiles at x = 296 mm are shown in Fig. 6. A deviation is visible in the inclination of the logarithmic part between experiment and numerical calculations. Also at the edge of the boundary layer a deviation from the experiment is visible, which is largest for the MSST model. This deviation corresponds to the lower shear stress that was already visible in Fig. 4.

Analysis shows that the calculation of the boundary layer thickness is also very different for the 4 tested models. In Table 1 the results for the prediction of the boundary layer thickness taken at x = 296 mm are summarised. It can be seen that the absolute boundary layer thickness of the SA-E model is closest to the experimental result and also in the normalised boundary layer profile the slight S-shape of the curve is visible where all other models turn out to be more flat in the shape of the curve. Nevertheless, the boundary layer height is underpredicted for all cases.

Looking at the wall pressure, significant differences between simulation and experiment can be seen. In the vicinity of the shock impingement point on the flat plate, the surface pressure increases and a separation bubble is formed (Fig. 7). The predicted absolute size of this separation bubble is smaller than the experimental value for all applied turbulence models. Due to the neglect of the boundary layer on the shock generator in the CFD computations the shock impinges slightly more downstream than in the experiment (Fig. 5). However, this small deviation does not explain the differences in the surface pressure distributions between the experiment and the CFD calculations. It is also under discussion that the adaptation process influences the position of the separation point when separation is not forced by geometry. Despite the fact that separation is triggered by the shock generator with shock impingement on a fixed position, another calculation was performed (not shown here) with a pre-refined grid and no adaptation, but the surface pressure distribution remained unchanged.

In Table 1 the point of separation and the relative size of the separation bubble are given for the numerical calculations in comparison to the experiment. Also from Fig. 8 can be seen that the SA-E turbulence model, which was best in the prediction of the boundary layer thickness, is the worst in the prediction of the separation point where c_f turns zero, whereas especially the TNT model, which has been poorer in the prediction of the boundary layer thickness, predicts a better point and relative size of the separation. However, the lower wall shear stress demands a bigger separation zone but also with the exception of the TNT model where the relative size of separation is bigger than in the experiment, all other models do underpredict this size, herewith revealing an inconsistency. Interestingly, the relative size of the separation bubble is only underpredicted for the case of the strongest interaction (deflection angle 14°) and overpredicted for the deflection angles of 10° and 6°. Also striking in this graph and this also holds for the diagram of Stanton numbers as well, are the huge visible differences in the numerical calculations from the experiment in the wake downstream of the interaction. The agreement between experiment and calculation for both parameters is fair in the undisturbed turbulent region and basically not given at all in the wake.

From results not shown here it was also concluded that an increase of the external turbulence intensity shifts the separation and re-attachment point slightly downstream, as is to be expected from a more turbulent flow. This finding is also in agreement with a review article [6] and also [1], where the same experiment was taken as basis for comparisons with numerical simulations but with focus on the influence of external turbulence levels and also shock unsteadiness on the separation point.

The prediction of the heat flux matches very well the experiment in the area of the turbulent undisturbed flow. In fact, all turbulence models do show the same level here (Fig. 9). Additionally, the SA-E provides as the only model a peak with increasing values in the separation point where all other turbulence models show a decrease in the heat flux. From the experiment it can be seen that as soon as the pressure increases underneath the separation shock, the heat flux increases as well. In the numerical simulation it shows a sharp decrease before the actual rise of the heat flux occurs in the re-attachment point, but the plateau within the separation zone is not caught numerically. This was also the case in [10], who also simulated this experiment and investigated the effect of compressibility corrections. The re-attachment point is also over-predicted by most models, again with the exception of the SA-E model which actually follows as the only model the experimental curve very well.

For the 6° and 10° case the grids were changed to a reduced height in the area of the expected separation. So the automatic adaptation process could condense the grid cells in the area where it was needed. But despite the assumption that the change in the grid structure of the boundary layer would improve the prediction quality, the deviation of the 10° and 6° cases did not vanish or even decrease. Fig. 10 shows the pressure distributions with good agreement in the undisturbed part of the plate, the already known bad separation behaviour and also deviations in the wake flow, where the 14° show a better agreement. The result in terms of prediction of separation and re-attachment can be

seen in Table 2, Table 3, and Fig. 11. The relative separation length of the 10° case is even increasing to about 40% (3.77) although it has to be kept in mind that the separation zone is smaller due to the weaker interaction and herewith the deviations carry more weight. In the 6° case where the experiment shows attached flow over the whole plate, the numerical simulation shows separation, even with the SA-E model which separates not as quick as the also applied MSST model. This is in contrast to [1] and [10] who both showed the attached flow in the simulation of the 6° case, [1] with the 2-equation model of Wilcox and [10] with Wilcox and also the MSST model. On the other hand it has to be mentioned that a micro-separation of the size of the numerical prediction would be a very difficult task to resolve in the experiment, if not impossible. Somewhere around this deflection angle, separation begins to take place, the numerical prediction can be right or wrong in this point.

In Fig. 12 it becomes obvious that the overshoot in heat flux downstream of the re-attachment point of the MSST model is much less pronounced in the 6° case, so it can be seen that it is related to the intensity of the interaction what seems to be plausible, but here we also see an overshoot for the SA-E model, which did not show this overshoot in the 14° case, indicating that it might have been pure coincidence that the 14° case was in such a good agreement.

Conclusions

A wind tunnel experiment was used to assess the CFD prediction of heat flux and skin friction for the case of shock impingement on a flat plate under three deflection angles of 14°, 10°, and 6°. It was shown that for the correct simulation of the heat flux in the undisturbed turbulent boundary layer it is necessary to provide a grid a with first wall-normal spacing of a y^+ of significantly smaller than 1 which is the value aspired for turbulence modelling. Here, good results were achieved with a y^+ of about 0.1, but it could not be concluded from these calculations, where the threshold value is. Additionally, it can be seen that if the general turbulence intensity is known from the experiment, it is favourable to perform the calculations with this value as the turbulence level of course is contributing to the heat flux on the wall.

The different turbulence models agree well in the undisturbed area but show significant variations in all parameters in and around the interaction region, e.g. boundary layer thickness, separation and re-attachment points, so there is no one model which provides the best prediction of all parameters; SA-E provides very good agreement in the heat flux for the 14° case but shows deviations in all other parameters discussed similar to the other models. Also the boundary layer thickness is close to the experiment in the SA-E model, but e.g. the ability to predict separation is poor where MSST or EARSM do a better job. Significant deviations can be seen in all parameters in the wake of the interaction; here the different turbulence models had considerable difficulties.

However, the results of the different parameters discussed and currently implemented version of the models used show an inconsistency in the wall shear stress that gives space for further improvement of the formulation of the according models.

References

[1] Fedorova, NN, Fedorchenko, IA, Computations of Interaction of an Incident Oblique Shock Wave with a Turbulent Boundary Layer on a Flat Plate, Journal of Applied Mechanics and Technical Physics, Vol. 45, No. 3, pp 358-366, 2004

[2] Mack, A., Hannemann, V., Validation of the Unstructured DLR-TAU-Code for Hypersonic Flows, AIAA 2002-3111, 2002

[3] Schülein, E., Krogmann, P., Stanewsky, E., Documentation of two-dimensional impinging shock/turbulent boundary layer interaction flow, DLR Report, IB 223 - 96 A 49, 1996, 69 p.

[4] Reimann, B., Johnston, I., Hannemann, V., The DLR TAU-Code for High Enthalpy Flows, Notes on Numerical Fluid Mechanics and Multidisciplinary Design, Vol. 87, Springer, 2004

[5] Reimann, B., Martinez, J., Numerical and Experimental Investigation of a Hypersonic Glider, 37th AIAA Fluid Dynamics Conference and Exhibit, June 25-28, Miami, FL, 2007

[6] Roy, CJ, Blottner, FG, Review and Assessment of Turbulence Models for Hypersonic Flows, Progress in Aerospace Sciences 42, pp 469-530, 2006

[7] Schülein, E., Skin-Friction and Heat Flux Measurements in Shock/Boundary-Layer Interaction Flows, AIAA Journal Vol. 44, pp 1732-1741, 2006

[8] Schwamborn, D., Gerhold, T., Kessler, R., The DLR TAU Code - an Overview, Proceedings ODAS 99 ONERA-DLR Aerospace Symposium, Paris, France, 21-24 June, 1999

[9] Young, AD, Modern Developments in Fluid Mechanics, High Speed Flow, (ed. L. Howath), Vol. 1, pp 375-475, Clarendon Press, Oxford, 1953

[10]Steelant, J., Effect of a Compressibility Correction on Different Turbulence Models, *Engineering Turbulence Modelling and Experiments 5*, edited by W. Rodi and N. Fueyo, pp.207-216, Elsevier, 2002

Tables

14°	Experiment	MSST	TNT	EARSM	SA-E
δ [mm]	4.10	3.41 (-16.8%)	3.26 (-20.5%)	3.85 (-6%)	4.07 (-0.7%)
Separ. [mm]	314.0	325.13	321.75	325.75	332.38
Re-att. [mm]	347.0	351.7	351.63	351.25	354.0
Size of sep. bubble [mm]	33.0	26.57	29.88	25.5	21.62
Relative size of sep. bubble L/δ [−]	8.05	7.79 (-3.2%)	9.17 (+13.9%)	6.62 (-17.8%)	5.31 (-34.0%)

Table 1   Comparison of undisturbed boundary layer thickness, separation and re-attachment point of the experiment and the four different turbulence models for the shock deflection angle of 14°. The values in brackets state the deviation in percent from the experiment.

10°	Experiment	MSST
δ [mm]	4.10	3.41 (-16.8%)
Separ. [mm]	334.0	337.13
Re-att. [mm]	345.0	350.0
Size of sep. bubble [mm]	11	12.87
Relative size of sep. bubble L/δ [−]	2.68	3.77 (+40.7%)

Table 2   Comparison of undisturbed boundary layer thickness, separation and re-attachment point of the experiment for the shock deflection angle of 10° calculated with the MSST model. The values in brackets state the deviation in percent from the experiment.

6°	Experiment	SA-E	MSST
δ [mm]	4.10	4.05 (-1.2%)	3.41 (-16.8%)
Separ. [mm]	-	347.0	345.94
Re-att. [mm]	-	347.8	348.88
Size of sep. bubble [mm]	-	0.8	2.94
Relative size of sep. bubble L/δ [−]	-	0.2	0.86

Table 3   Comparison of undisturbed boundary layer thickness, separation and re-attachment point of the experiment for the shock deflection angle of 6°, calculated with the SA-E and the MSST model. The values in brackets state the deviation in percent from the experiment.
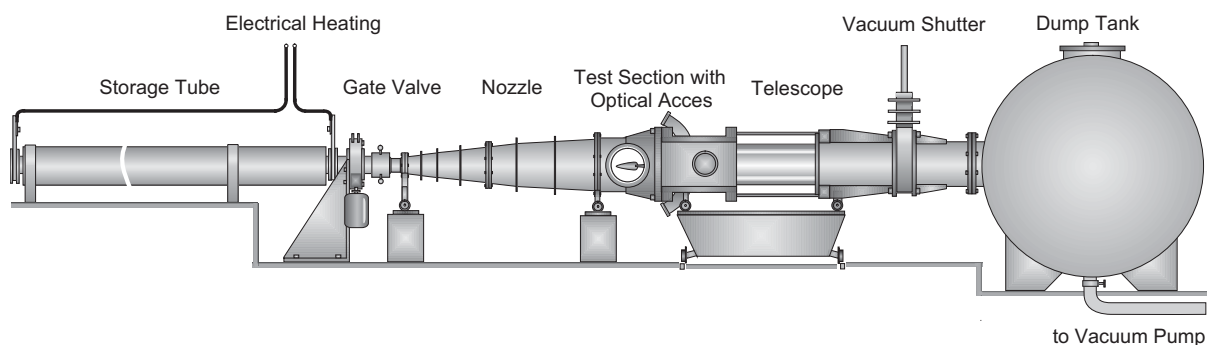
Figures

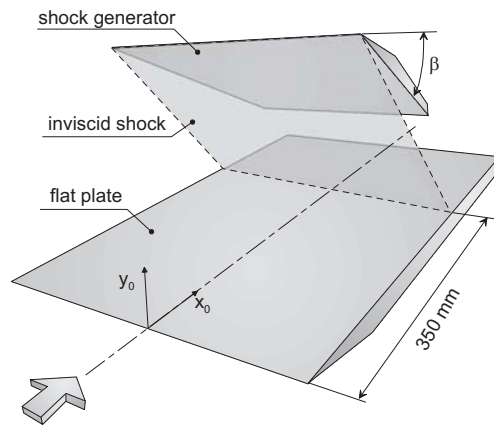**Fig. 1   Sketch of the Ludwieg Tube Facility (RWG).**

Fig. 2   Sketch of the test model.
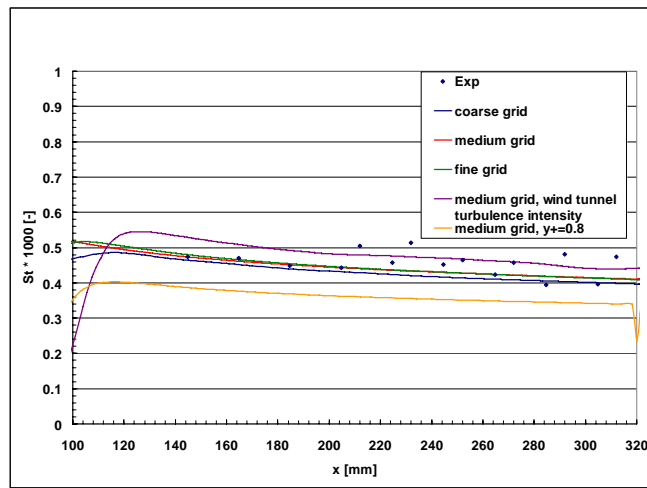

Fig. 3   Comparison of heat flux calculated on a coarse, medium, and fine grid with the experimental data.
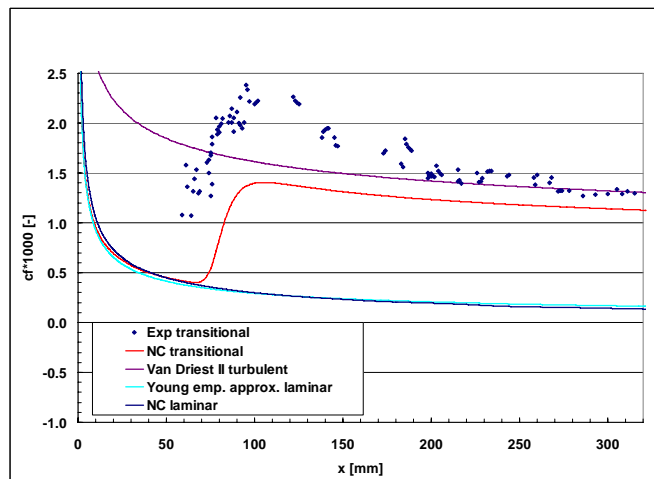

Fig. 4   Comparison of skin friction of the experiment with laminar and transitional numerical calculations (NC), the analytical laminar solution derived by Young, and the turbulent solution derived by Van Driest.
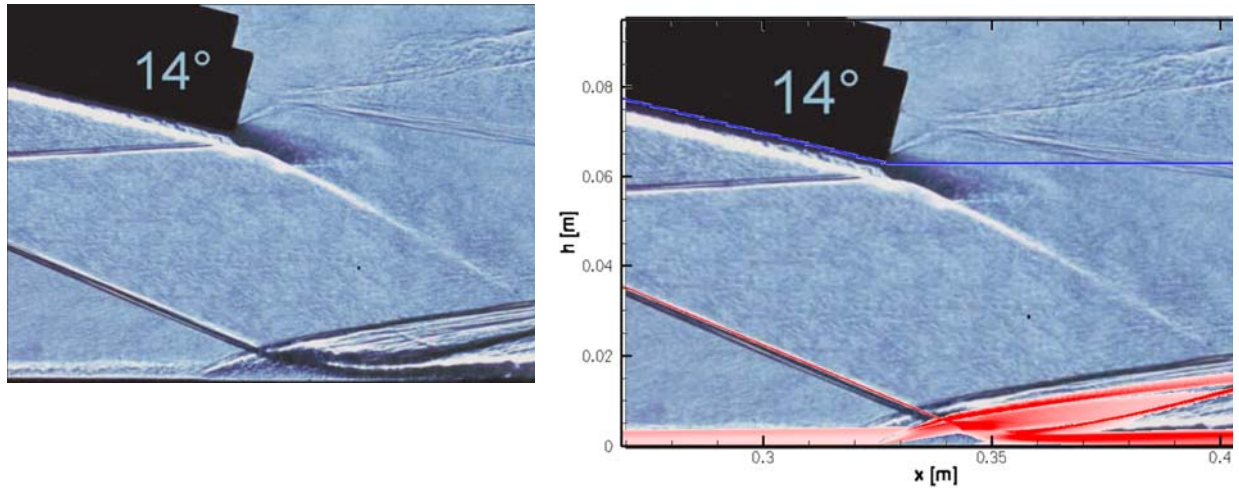
Fig. 5   Shadowgraph visualisation of the flow field in the vicinity of the SWTBLI (left) and overlaying numerical contours of the density gradient magnitude (right)
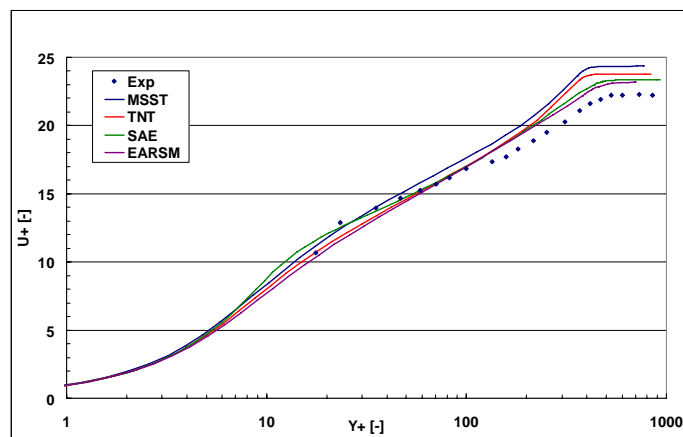
Fig. 6   Comparison of the normalised boundary layer profiles of the experiment and the different applied turbulence models at x=296 mm.
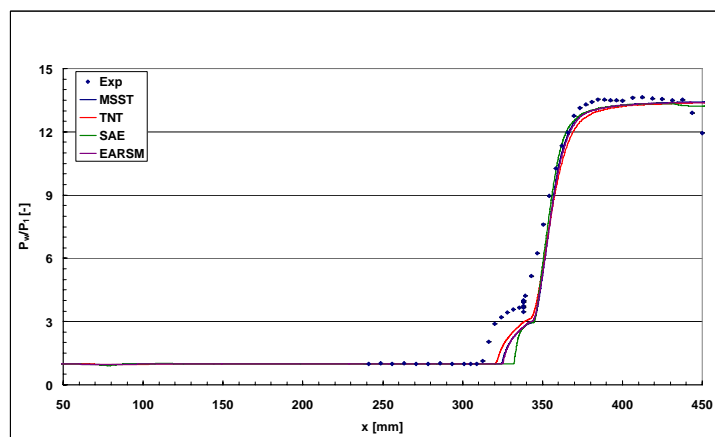
Fig. 7   Comparison of the measured and calculated surface pressure for the deflection angle of 14°. Experimental values with error-bars.
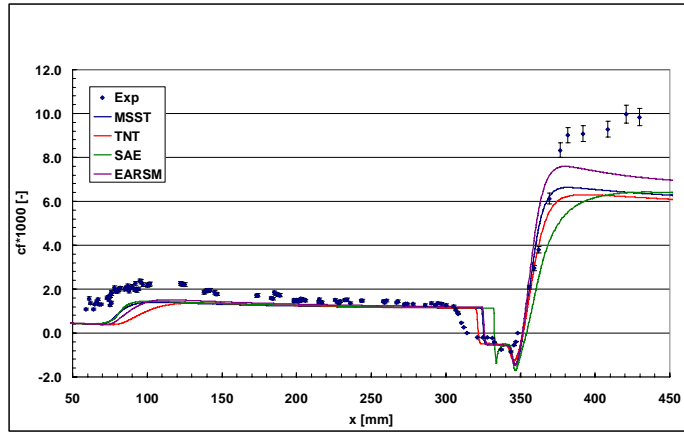
Fig. 8   Skin friction distribution for the deflection angle of 14°. Experimental values with error-bars.
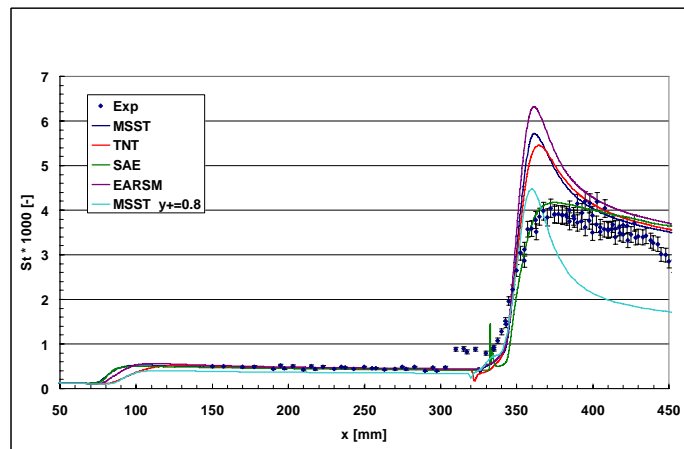
Fig. 9   Comparison of the heat flux for the deflection angle of 14°, displayed as non-dimensional Stanton number. Experimental values with error-bars.
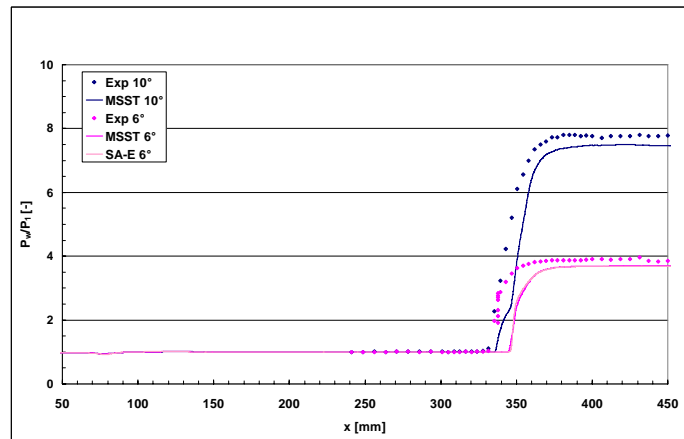

Fig. 10   Comparison of the measured and calculated surface pressure for the deflection angles of 10° and 6°.
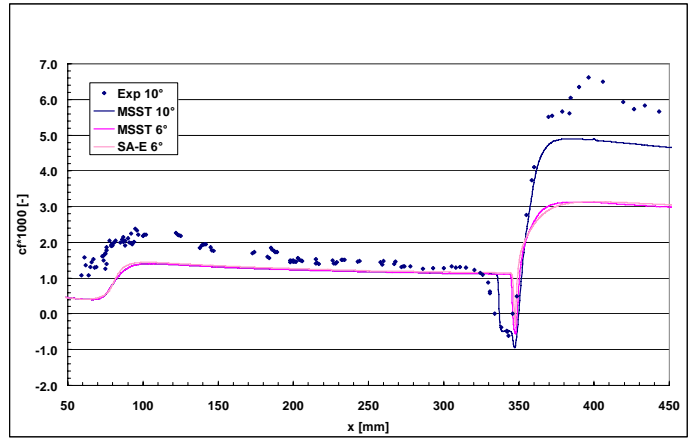
Fig. 11   Skin friction distributions for the deflection angles of 10° and 6°.
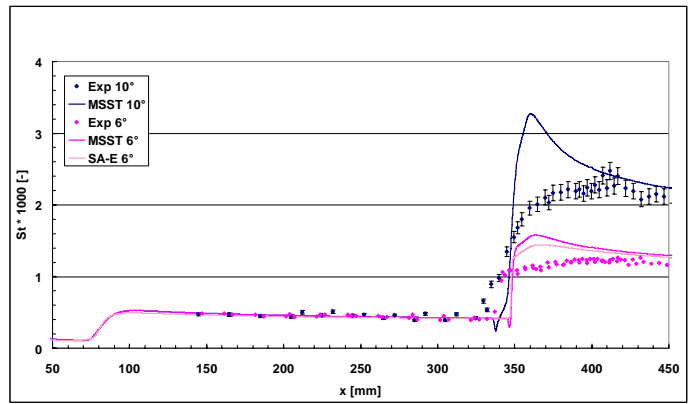

Fig. 12   Comparison of the heat flux, displayed as non-dimensional Stanton number of deflection angles of 10° and 6°. Experimental values with error-bars.